

## Carbonitriding of low alloy steels: Mechanical and metallurgical responses

W. Dal'Maz Silva<sup>a,b,\*</sup>, J. Dulcy<sup>a</sup>, J. Ghanbaja<sup>a</sup>, A. Redjaïmia<sup>a</sup>, G. Michel<sup>b</sup>, S. Thibault<sup>c</sup>, T. Belmonte<sup>a</sup>

<sup>a</sup> Institut Jean Lamour – UMR CNRS–Université de Lorraine, 7198, Parc de Saurupt, Nancy 54011, France

<sup>b</sup> Institut de Recherche Technologique M2P, Metz 57070, France

<sup>c</sup> Safran Tech, Magny les Hameaux, France



### ARTICLE INFO

**Keywords:**

Hardness measurement

Martensite

Low-alloy steel

Precipitation

### ABSTRACT

Metallurgical and mechanical responses of alloys 16NiCrMo13 and 23MnCrMo5 to the addition of carbon and/or nitrogen were investigated. Diffusion profiles of these interstitial elements were established by atmospheric pressure carburizing, austenitic nitriding, and a sequence of carburizing and nitriding – the carbonitriding. All treatments were performed at 1173 K under CO-H<sub>2</sub> and/or NH<sub>3</sub> based atmospheres. After enrichment, each sample was (i) room-temperature oil-quenched and (ii) immersed in boiling nitrogen prior to (iii) the stress relief treatment. Cross-section hardness profiles were evaluated after each of these steps. Electron probe microanalysis (EPMA) allowed for the determination of both carbon and nitrogen diffusion profiles after quenching. In order to estimate the fraction of nitrides formed during the enrichment of the alloys, these measured profiles were employed in the simulation of local equilibrium at each evaluated position. This allowed for the computation of total solid solution interstitial content, which was expressed in atomic fraction. Plots of as-quenched hardness against the square root of the computed interstitial content, i.e. the sum of solution carbon and the remaining nitrogen, show the complementary character of these elements in determining the mechanical properties of the materials prior to stress relief treatment. Tempering of carbon-nitrogen martensite resulted in hardness drop to a lesser degree than the one measured on carbon martensite with equivalent interstitial content. In order to investigate this behavior, transmission electron microscopy (TEM) analyses were performed. Results showed the precipitation of two morphologies of Fe<sub>16</sub>N<sub>2</sub> in the nitrogen-rich case and image analysis confirmed the simulated fraction of nitrides.

### Introduction

Carbonitriding is an austenitic field case hardening process generally conducted from 1073 K to 1173 K [1,2] through the introduction of carbon and nitrogen into iron, low-carbon low-alloy steels, and powder metallurgical parts. It is often performed on power transmission components, such as gears, which are submitted to structural and surface fatigue operating conditions. Aiming at the required properties, carbonitrided parts are quenched [3] to outcome the strain energy required by martensite transformation [4]. This leads to a hard and brittle lath martensite microstructure, which is typically tempered prior to application. Thus, the understanding of attainable mechanical properties is based on carbon-nitrogen martensite behavior. Conversely to nitrogen effects [5,6], much has been reported about the role of carbon on martensite transformation of steels [7]. For nitrogen martensite, literature remains mostly limited to the Fe–N system, for which metallurgical transforma-

tions through tempering and room temperature aging are established [8–15]. Although the behavior of as-quenched carbon-martensite can be readily described in terms of interstitial content [7,16–18], the role of nitrogen as an interstitial atom are not often reported. It has been proposed that for typical treatment durations, precipitation of nitrides does not reach the equilibrium fractions computed with some of the currently available thermodynamic databases [5]. Thus, elemental partitioning [19] between matrix and nitrides formed during alloy enrichment plays a role on the nature and fractions of possible phases formed during tempering.

The objectives of this paper is to explore metallurgical responses rather than process parameters, which are discussed in reference papers [1,20]. This work focuses on carbonitriding as a sequence of carburizing and nitriding steps, although simultaneous enrichment in both interstitial elements is the long-term established industrial practice of atmospheric pressure process [1]. Nitrogen solubility at treatment temperature is

\* Corresponding author at: Institut Jean Lamour – UMR CNRS–Université de Lorraine 7198, Parc de Saurupt, Nancy 54011, France.

E-mail addresses: [waltermateriais@me.com](mailto:waltermateriais@me.com) (W. Dal'Maz Silva), [jacky.dulcy@univ-lorraine.fr](mailto:jacky.dulcy@univ-lorraine.fr) (J. Dulcy), [jaafar.ghanbaja@univ-lorraine.fr](mailto:jaafar.ghanbaja@univ-lorraine.fr) (J. Ghanbaja), [abdelkrim.redjaïmia@univ-lorraine.fr](mailto:abdelkrim.redjaïmia@univ-lorraine.fr) (A. Redjaïmia), [gregory.michel@irt-m2p.fr](mailto:gregory.michel@irt-m2p.fr) (G. Michel), [simon.thibault@safran.fr](mailto:simon.thibault@safran.fr) (S. Thibault), [thierry.belmonte@univ-lorraine.fr](mailto:thierry.belmonte@univ-lorraine.fr) (T. Belmonte).

drastically reduced by the presence of alloying elements such as chromium and manganese and precipitation of nitrides takes place during the enrichment. Thus, the effective nitrogen hardening effect is proposed to be linked to the reminiscent interstitial nitrogen, which also reduces the critical cooling rate for quenching, leading to a more consistent martensite transformation. Experimental studies supported by Thermo-Calc [21,22] thermodynamic simulations of steels composition after treatments were conducted. Hardening responses to carburizing and austenitic nitriding are compared to carbonitriding results. Local hardnesses along the diffusion profiles are correlated to composition and microstructure. Thermo-Calc [21,22] simulations are used for predicting MN-nitrides precipitation along the diffusion profile, allowing for the incorporation of nitrogen in the hardening model [16,17].

## 1. Experimental methods

### 1.1. Treatment parameters

Metallurgical responses to thermochemical treatments – carburizing, austenitic nitriding and carbonitriding – of alloys given in Table 1 are studied. Specimens with dimensions of  $40 \times 14 \times 4$  mm taken from wrought bars are polished up to 1200 grit sandpaper prior to enrichment. Processing is then carried out in a vertical flow reactor with a diameter of 50 mm and 100 mm isothermal length at the setup temperature. Since the studied alloys do not contain intentionally added grain growth stabilizers, in order to optimize process kinetics without compromising austenitic grain size [23], a temperature of 1173 K is adopted for all treatments. Heating is carried out under inert atmosphere consisting of  $N_2-0.2H_2$  with total flow rate of  $500 \text{ cm}^3 \text{ min}^{-1}$ . A carburizing atmosphere based on  $CO-H_2$ , controlled through dew point measurement [24], has been designed to promote carbon surface saturation. Nitrogen enrichment is conducted through an ammonia-cracked-ammonia atmosphere. Diffusion steps, as well as tempering times and temperatures, are given in Table 2. After treatment, samples are immediately oil quenched (298 K) and submitted to cryogenic treatment in boiling nitrogen (77 K). Tempering is carried under the same atmospheric conditions employed during the heating stage.

### 1.2. Materials characterization

Treated samples are cross-sectioned and are mounted in epoxy resin (3 min at 433 K) prior to analyses. Grinding is followed by progressive alumina polishing until particle size below 0.5  $\mu\text{m}$ . Visible-light microscopy (VLM) assessment of microstructure and mechanical property measurement through Vickers micro-hardness testing under a load of 300 gf (HV0.3) are carried out. Chemical micro-analyses of diffusion profiles are conducted through Jeol JXA-8530F electron probe micro analyzer (EPMA) using the same calibration techniques described by Catteau et al. [5]. Identification of both high- and low-temperature precipitates, i.e. those formed during enrichment and those formed during temper, respectively, is performed through transmission electron microscopy (TEM) using a Jeol ARM-200F equipment operating at 200 kV. High temperature precipitates composition and size distributions are identified semi-quantitatively by energy dispersion x-ray spectroscopy (EDS) and the precipitates structure is identified by electron diffraction.

**Table 1**

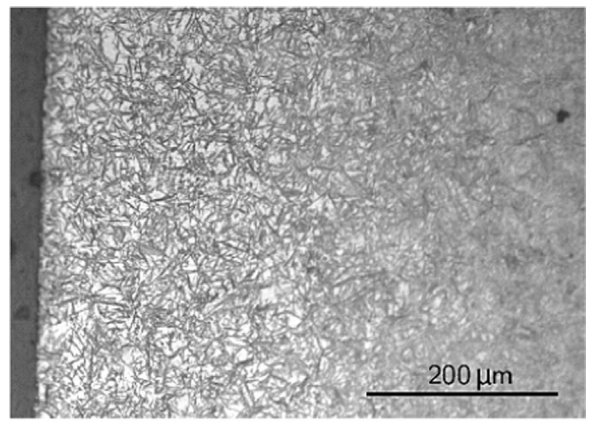
Nominal composition of the studied alloys (wt%).

Alloy	Fe	C	Si	Mn	Cr	Ni	Mo
16NiCrMo13	Bal.	0.16	0.25	0.45	1.00	3.20	0.25
23MnCrMo5	Bal.	0.23	0.25	1.20	1.30	0.20	0.25

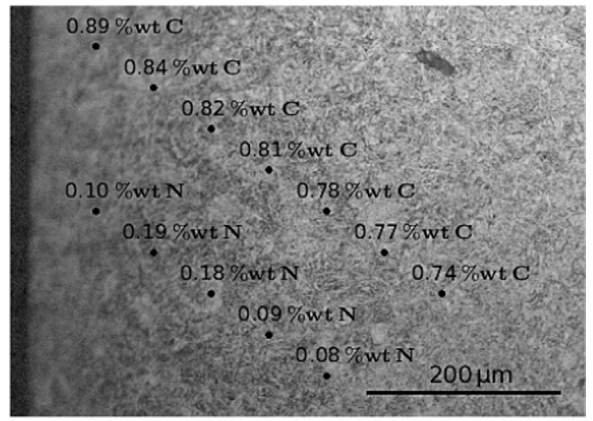
**Table 2**

Treatment durations for carburizing, austenitic nitriding and carbonitriding. In addition to the tempering conditions given on the table, nitrided samples were also tempered during 18 h at 673 K. Carbon enrichment is carried under an atmosphere composed of  $CO-H_2-N_2$ , diffusion and tempering steps under  $N_2-H_2$ , and nitrogen enrichment is carried under  $NH_3-H_2-N_2$ .

Treatment	Material	Enrichment/diffusion duration at 1173 K			Tempering ( $N_2-H_2$ )
		Carbon	Diffusion	Nitrogen	
Carburizing	16NiCrMo13	2 h	4 h	–	70 h at 453K
	23MnCrMo5	–	3 h	–	
Nitriding	Both	–	–	–	18 h at 573K
	16NiCrMo13	2 h	1 h	–	
	23MnCrMo5	–	–	3 h	



(a) After oil quenched



(b) After cryogenic treatment

**Fig. 1.** Visible light micrographs of alloy 16NiCrMo13, surface enriched with around 0.90 wt% C and 0.10 wt% N, after (a) oil quench at 298 K and (b) cryogenic treatment at 77 K. Composition along the profile is shown in figure. Magnification of 200 $\times$ . Image analysis of the zone comprised by the surface and a depth of 200  $\mu\text{m}$  in (a) reveals about 35% of residual austenite.

## 2. Results

Effects of cryogenic treatment over retained austenite ( $\gamma_r$ ) decomposition after carbonitriding of alloy 16NiCrMo13 are presented in Fig. 1, which shows equivalent regions before (Fig. 1a) and after (Fig. 1b) cryogenic treatment along with local composition. This representation is proposed in order to provide an understanding of  $\gamma_r$  content in terms of interstitial elements mass fractions and will later be related to the H-point

[15] composition. Quantitative VLM<sup>1</sup> image analysis of this cross-section before cryogenic treatment (Fig. 1a) indicates the presence of around 35% of  $\gamma_t$  in the region comprised between the surface and a depth of 200  $\mu\text{m}$ . Due to limitations of this technique,<sup>2</sup> no quantification was performed by image analysis after cryogenic treatment, condition (Fig. 1b) for which it is believed that  $\gamma_t$  content lies below 5% [25].

Fig. 2 presents the relationship between total nitrogen and reminiscent solid solution nitrogen, as well as the mass fraction of MN nitrides at 1173 K. These quantities are assumed to represent as-quenched martensite composition and will later be used in the analysis of its hardness profiles. Fig. 3 summarizes measured as well as simulated diffusion profiles for all treatment setups. Under the same operating conditions, i.e. same nitriding potential [26], surface nitrogen for alloy 16NiCrMo13 did not reach 0.4 wt% N while alloy 23MnCrMo5 exceeds 0.6 wt% N. In order to simulate carbonitriding profiles, a mass transfer coefficient was set to take decarburizing effect into account.

Experimental composition profiles are then used as input for local equilibrium computations at enrichment temperatures using Thermo-Calc [21,22] database TCFE7. Such simulations provide the total solid solution atomic fraction  $x_i$  for carbon and nitrogen, which is then used to plot hardness against  $x_i^{0.5}$ , the square root of this quantity, as shown in Fig. 4. As it will be explained later, this quantity  $x_i^{0.5}$  is expected by the underlining physics of the process [18]. This method makes no distinction between treatments since it is resorted to evidence the complementary character of interstitial elements. Three distinct behaviors are depicted in Fig. 4: (i) a linear dependence of hardness with  $x_i^{0.5}$  up to a value of 0.16 (corresponding to around 0.55 wt% of interstitials) (ii) a hardening plateau until around 0.19 (0.90 wt% of interstitials) and (iii) a strong hardness decrease for higher contents. These points beyond the so-called H-point were obtained from high carbon samples, which were quenched directly after enrichment for illustration purposes and correspond to the microstructure presented in Fig. 1. Next, Fig. 5 shows the behavior of hardness due to tempering effects for the samples quenched in boiling nitrogen with diffusion profiles given in Fig. 3. For alloy 16NiCrMo13 the maximum hardness attained by cryogenic quenching was around 750 HV0.3 while for alloy 23MnCrMo5, hardening reached 800 HV0.3. These start-points hardnesses are presented together with hardness profiles for samples tempered at both 453 K and 573 K. Hardness profiles for nitrided samples are presented in Fig. 6 with a detail of nitrogen diffusion profile to better depict the abnormal tempering effect observed for this treatment. Hardness is kept close to the as-quenched level in the nitrogen-rich zone (0.0–0.2 mm) if tempering is carried out above 573 K, while at 453 K hardness decreases as a whole. Treated materials are then studied by transmission electron microscopy. Fig. 7 presents chemical maps (EDS) of precipitates with dimensions of less than 1  $\mu\text{m}$  observed in a foil taken at 0.2 mm from the treated surface of alloy 23MnCrMo5 after carbonitriding. These maps present the main elements found to compose the precipitates, which include nitrogen, chromium, manganese and silicon. On the other hand, precipitates formed at enrichment temperatures during nitriding and carbonitriding for alloy 16NiCrMo13 show only significant amounts of nitrogen and chromium (Fig. 8). Finally, the abnormal behavior observed after tempering nitrided specimens of alloy 16NiCrMo13 is depicted in Fig. 6. This samples showed a lath martensite structure with characteristic width in the order of 200 nm, as depicted in Fig. 9. It is studied by comparing the reference as-quenched state microstructure (Fig. 10) with the sample tempered at 573 K (Fig. 11), comprising standard transmission micrographs, diffraction patterns (DP) and high resolution microscopy (HRTEM). Although both Fig. 10c and Fig. 11c present similar selected area diffraction patterns corresponding to  $\text{Fe}_{16}\text{N}_2$  precipitates, different sizes and morphologies are observed.

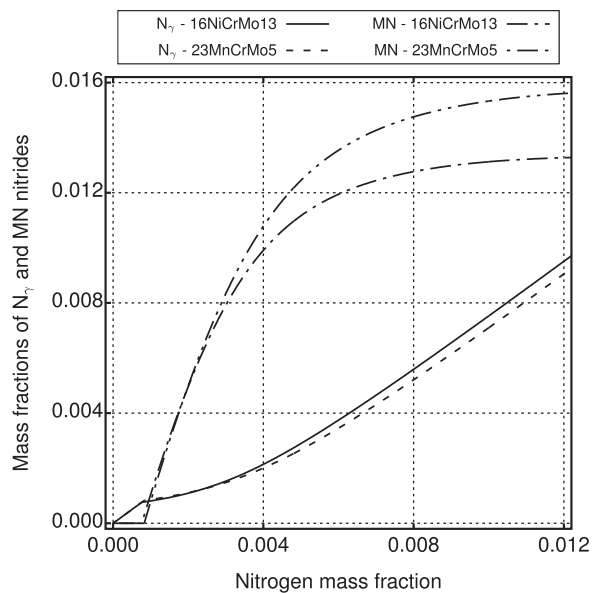


**Fig. 2.** Content of nitrogen in solid solution and volume fraction of nitrides in terms of total nitrogen content for alloys 16NiCrMo13 and 23MnCrMo5. Simulations were carried out with Thermo-Calc [21,22], database TCFE7 considering a carbon content of 0.4 wt% and temperature of 1173 K.

### 3. Discussion

Before proceeding with the analyses of diffusion profiles and their influence over mechanical properties, some knowledge about the equilibrium phases at enrichment temperature (1173 K) is desirable. Thermo-Calc [21,22] was used for the simulation of pseudo-equilibrium isothermal sections in terms of carbon and nitrogen contents. Using database TCFE7, carbon saturation at ~1.0 wt% is predicted for both alloys, above which  $\text{M}_3\text{C}$  is the equilibrium carbide, as reported for some of the ternary and quaternary systems closely related to the studied alloys [27–29]. The threshold for precipitation of nitrides is found around 0.10 wt% N in the absence of carbon and decreased slightly to 0.08 wt% N at carbon saturation. Since these computations are performed considering all the elements listed in Table 1, diagrams tie-lines are not in the calculation plane and thus, these limits for precipitation of carbides and nitrides are just thresholds above which further solubility of interstitials is still possible. To illustrate this, Fig. 2 presents the content of nitrogen in solid solution along with MN nitride volume fraction in terms of total nitrogen content. Increasing the nitrogen content above the precipitation threshold leads to increasing the nitrogen solubility: the alloy behavior approaches the iron-like solubility limit due to the depletion of alloying elements from the matrix. Simulations show that up to a certain limit,<sup>3</sup> only MN (M=Cr, Mo) nitrides are present, while higher contents lead to the precipitation of  $\text{Si}_3\text{N}_4$ , as expected in the iron-rich corner for the Fe-Si-N system [30]. Precipitation is accompanied by the depletion of alloying elements from the matrix, leading to increased nitrogen solubility, i.e. the austenitic matrix tends towards the Fe-N system behavior. Due to their size – sub-micrometer scale – and morphology kinetically favored by treatment temperature, these nitrides are incoherent with the matrix and do not represent a dislocation glide barrier.

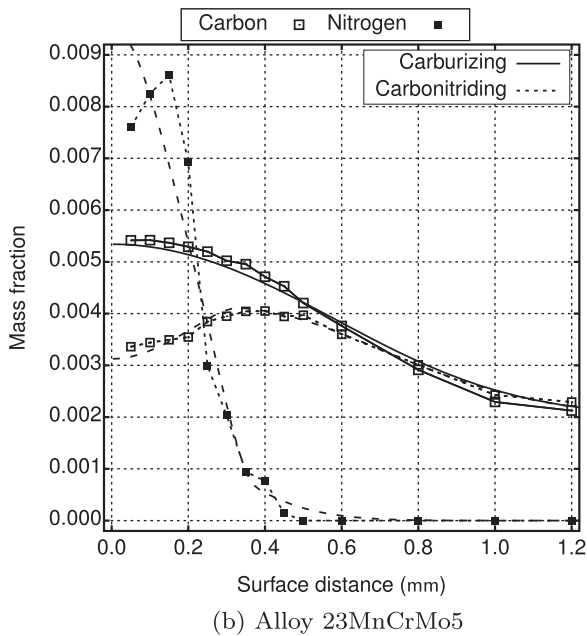
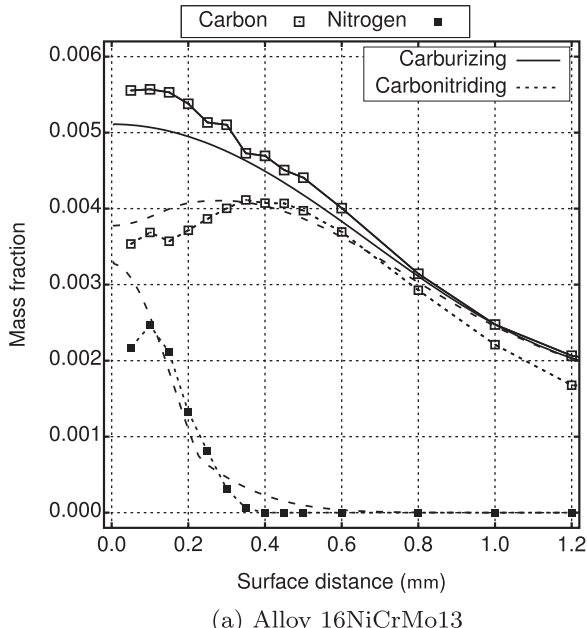
#### 3.1. Diffusion profiles

Fig. 3 presents the intricate behavior of carbon and nitrogen diffusing simultaneously during carbonitriding when compared with the single-phase diffusion of carbon during carburizing. Processing conditions led to diffusion profiles in good agreement with Thermo-Calc [21,22] simulations

<sup>1</sup> Visible light microscopy.

<sup>2</sup> Actually, even with XRD the quantification of  $\gamma_t$  becomes difficult if the micrographs do not show any considerable amount of this component [25].

<sup>3</sup> Below 0.5wt%N in the range of carbon contents achieved in the present work.



**Fig. 3.** Carbon and nitrogen diffusion profiles : (a) alloy16NiCrMo13 and (b) alloy 23Mn-CrMo5. Full lines without markers represent the simulated profiles. Simulations were carried out with Thermo-Calc [21,22], databases TCFE7 and MOBFE2.

for carburizing. On the other hand, carbonitriding is not properly modeled simply by constant surface activity boundary conditions derived from atmosphere thermodynamics, i.e. saturation activity for carbon and atmosphere nitrogen activity, requiring decarburizing to be taken into consideration. The carbon maximum observed for both alloys in the carbonitriding simulations around 0.3 mm from the surface is also related to the repulsion of interstitial elements between themselves, i.e. carbon-carbon, nitrogen-nitrogen and nitrogen-carbon negative interacting energies. The formation of methane was put into evidence by monitoring the process by gas chromatography. Based on the measurement of this hydrocarbon output, the surface reaction rate is estimated and implemented as the boundary condition for carbon back-flow in order to properly simulate carbonitriding diffusion profiles.

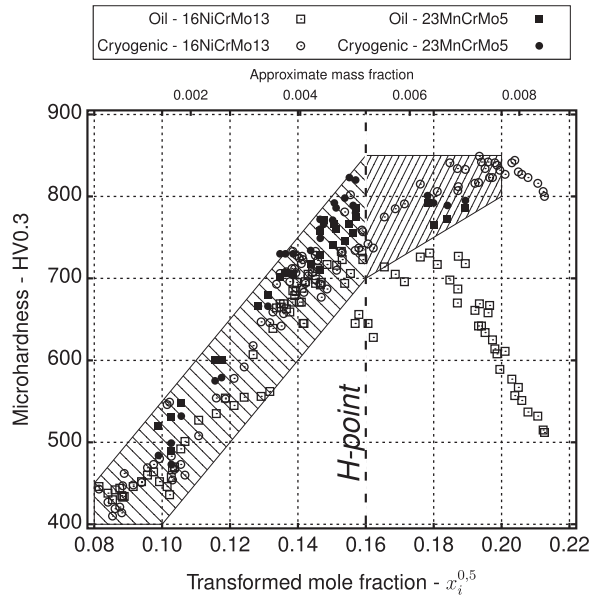
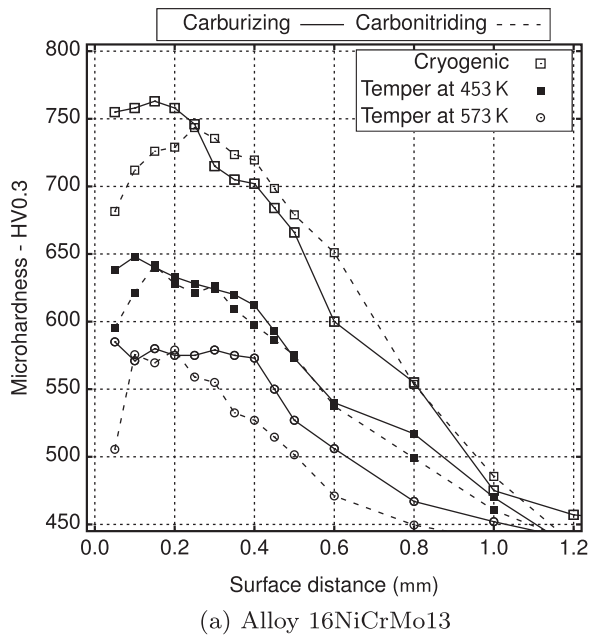


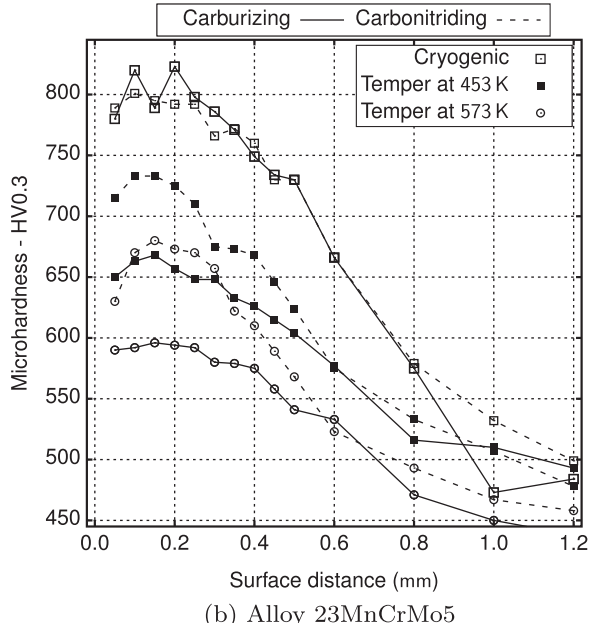
**Fig. 4.** Dependence of hardness on the square root of total interstitial content  $x_i^{0.5}$ . This plot shows the validity of the hardening model below the H-point for alloys 16NiCrMo13 and 23MnCrMo5. Above H-point, increasing amounts of retained austenite govern the global behavior.

Carbon-carbon repulsion behavior is well-known and reported in the literature [31–34]. In order to allow the simulation of such phenomenon and the interactions between alloying elements and interstitial atoms, Onsager [35,36] linear approach for irreversible thermodynamics is taken into account by Thermo-Calc [21,22]. Reasonably similar results may be achieved by integrating the diffusion equation following the approach of Slycke and Ericsson [2] for the Fe–C–N system. This approach takes into account the dependencies of the diffusion coefficients with interstitial contents only through geometric exclusion formalism. This implies that for low alloy steels, interaction energies among interstitial elements are much higher than with alloying elements, which play a major role only on blocking diffusion by formation of precipitates. Using the composition-independent carbon diffusion coefficient in austenite supplied by Slycke and Ericsson [2], it can be shown, for instance, with a Crank-Nicolson [37] scheme, that the pre-exponential factor needs to be multiplied by a factor of 1.8–2.0 in order to produce the same mass intake as Thermo-Calc [21,22] simulated values, in agreement with a discussion by Bhadeshia [31]. It means that C–C interactions can almost double the carbon diffusion coefficient with respect to its infinite dilution limit, i.e. in absence of carbon.

Measurements of residual ammonia at reactor outlet allow the computation of nitrogen activity  $a_N$  around 40, by taking atmospheric pressure N<sub>2</sub> as the reference state and equilibrium expressions given by Slycke and Ericsson [1]. This value was initially used for establishing the boundary condition for nitriding steps simulations, reasonably representing nitrogen profiles for alloy 23MnCrMo5. Regarding alloy 16NiCrMo13, this activity does not allow proper simulation of diffusion profiles, which are best fit by a nitrogen activity in the order of 10. This might be due to the catalytic effect of nickel favoring the recombination of adsorbed nitrogen atoms and formation of N<sub>2</sub> or other gas phase products. Additionally, the mass transfer coefficient required to properly fit the decarburizing profile observed for alloy 23MnCrMo5 is around 1.7 times the one needed for alloy 16NiCrMo13, reinforcing the catalytic effect hypothesis. Since decarburizing is slower for the later, then surface recombination processes are favored with regard to surface reaction with carbon uptake. Due to this deviation, nitrogen in solid solution is computed from the actual measured total nitrogen content in order to be incorporated in the hardening model.



(a) Alloy 16NiCrMo13



(b) Alloy 23MnCrMo5

**Fig. 5.** Hardness profiles after cryogenic treatment and after tempering for alloys (a) 16Ni-CrMo13 and (b) 23MnCrMo5. Reference state was chosen to be the hardness after cryogenic treatment since all parts were submitted oil-quench and to immersion in boiling nitrogen prior to stress relief.

### 3.2. As-quenched hardness

Hardness profiles of as-quenched martensite presented in Fig. 5 agree with typical reported values [38,7,18,39] for plain iron and low-alloy steels. Although this property is dependent on several factors such as martensite morphology, solid solution hardening and dislocation density and mobility [7], its strongest dependence relies on interstitial content, allowing direct comparison among iron-based materials [38,18]. For instance, Hutchinson et al. [18] show that for Fe-1.7Mn-0.23Si-0.12C and Fe-1.7Mn-0.21Cr-0.23Si-0.23C steels, the contribution of base alloying elements represents 10–12% of the yield strength. The grain size corresponds to about 13%, dislocations to 12–13%, martensite structure to 35–39% and (solid solution) interstitial atoms to 61–66%. It is assumed that the reasoning of the authors [18] was based on the idea that interstitial atoms behave as if they were solid

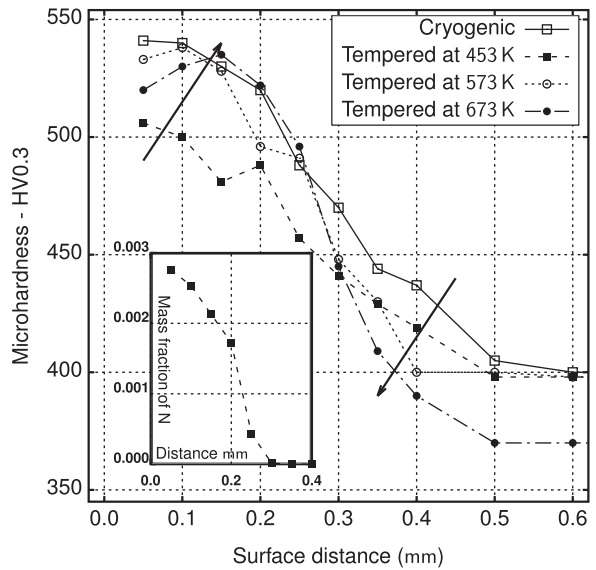


**Fig. 6.** Hardness profiles after cryogenic treatment and different tempering conditions for alloy 16NiCrMo13 nitrided. Arrows indicate the displacement of the maximum hardness toward the core with increasing stress relief temperature on the nitrogen-rich depth and the associated hardness drop beyond nitrogen reach.

solution clusters, blocking dislocation movement thanks to precipitates, and thus contributing to strengthening by a square-root dependence on their content [40]. Morito et al. [41] show a linear dependence of dislocation density on carbon content. Since dislocation forest strengthening is also represented by a square-root law versus dislocation density, this term in the total strengthening also obeys a square-root dependence with interstitial content [16,17,7,18].

We speculate that a similar behavior may be attributed to nitrogen in solid solution below what is known as the H-point, i.e. the composition at which BCC to BCT martensite transition occurs, since it happens at the same atomic fraction for both carbon and nitrogen [15]. Thus, the relationship proposed by Norstrom [17] may be generalized by considering the total mole fraction  $x_i$  of solid solution carbon and nitrogen, i.e. the amounts of these elements that are not under the form of precipitates. The knowledge of actual nitrogen in solid solution is necessary so that this element may be introduced in the model. Thermo-Calc [21,22] was used in the computation of the total interstitial mole fraction at each point where chemical microanalysis has been performed. Other contributions, such as depletion of alloying elements from the matrix or changes in martensite structure were considered irrelevant. Fig. 4 presents the plot of hardness versus  $x_i^{0.5}$ .

Such behavior for both elements seems logical if we consider the dislocation blocking in terms of clusters of interstitials, which must increase with the relative number of interstitial atoms in the structure, since the number of barriers to dislocation movement is the actual variable governing hardness [40]. Furthermore, as depicted by Yahia [42], the size of nitrogen in austenite is only about 5–7% larger than carbon. Thus, on the average it is expected a close blocking effect for both elements. An exhaustive study could allow the introduction of a coefficient for relative nitrogen effect, thus refining this model. Two main regions characterize plots in Fig. 4, the first where hardness increases linearly with increasing parameter  $x_i^{0.5}$  followed by hardening plateau. A straight line is added in order to highlight the zone where proportionality prevails, which has its upper boundary at  $x_i^{0.5} = 0.16$  before cryogenic treatment. This value may roughly be converted to  $w_C + w_N = 0.0055$  (0.55 wt%), above which no surface improvement may be achieved with room temperature oil-quench, corresponding to the well-known H-point [15]. A third region may be considered for highly enriched areas ( $x_i^{0.5} > 0.18$ ) at which hardness drastically decreases due to the fast growth in the amount of  $\gamma_r$  [15]. The decomposition of  $\gamma_r$  with cryogenic treatment is brought to light for alloy 16NiCrMo13 in Fig. 4 by the increase in hardness produced by its transformation into martensite. No such

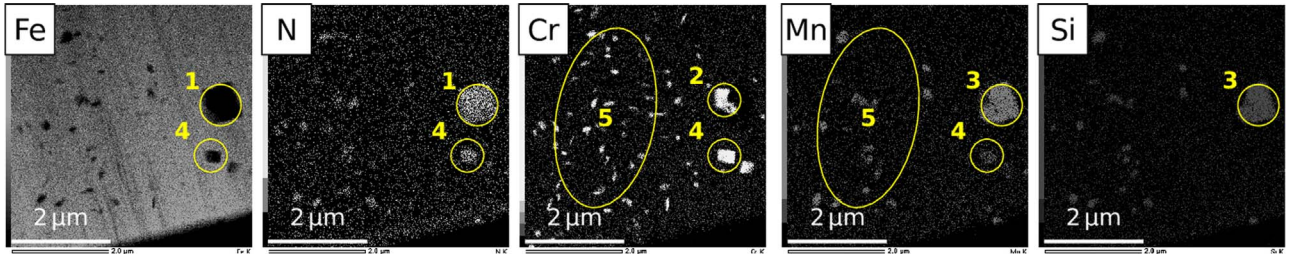


**Fig. 7.** Energy dispersive x-ray maps of nitrides formed during carbonitriding of alloy 23MnCrMo5. Nitrogen content around 0.80 wt%. Corresponding particles/regions are identified by the same number on different x-ray fluorescence cartographies. Point 1 denotes an iron-depleted area with corresponding nitrogen accumulation. This area contains nitrides 2 (MN, with M mostly Cr) and 3 ( $MnSiN_2$ ). Region 4 also shows a MN nitride, but in this case chromium is partially replaced by manganese. A multitude of small MN nitrides is present on region 5.

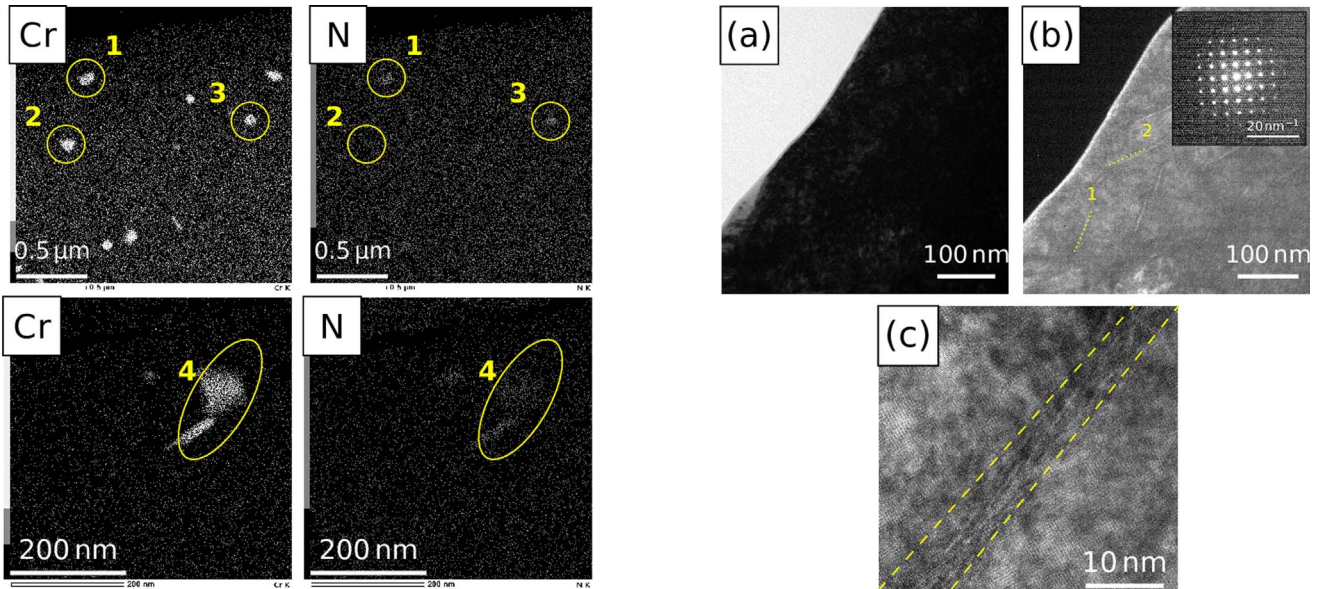


**Fig. 8.** Energy dispersive x-ray maps of nitrides formed during nitriding of alloy 16NiCrMo13 depicting (left) chromium rich zones and (right) their coincidence with nitrogen agglomeration. Nitrogen content around 0.25 wt%. Regions 1, 3, and 4 depict areas where both chromium and nitrogen were detected. Intensity of nitrogen x-ray fluorescence in region 2 was to low for detection.

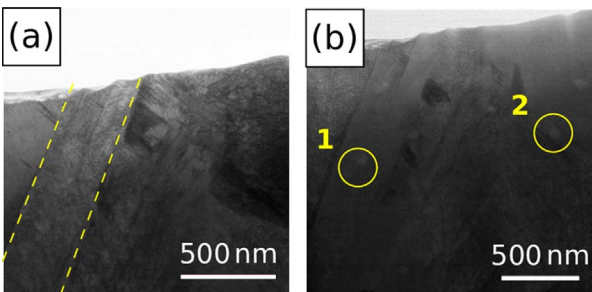


**Fig. 9.** Micrographs of alloy 16NiCrMo13 nitrided, quenched and submitted to cryogenic treatment : (a) bright field (BF) showing the lath martensite structure, with a lath boundaries marked by dashed lines, (b) the same but with high temperature MN nitrides better depicted and circumscribed.

phenomenon has been observed for alloy 23MnCrMo5 since it has not been enriched to high levels of interstitials.

### 3.3. Tempering effects

While the as-quenched hardness may be explained in terms of interstitial content, tempering produces a series of more complex phenomena leading to a decrement in hardness, as depicted in Fig. 5 where hardness after cryogenic treatment is chosen as reference state. Hardness

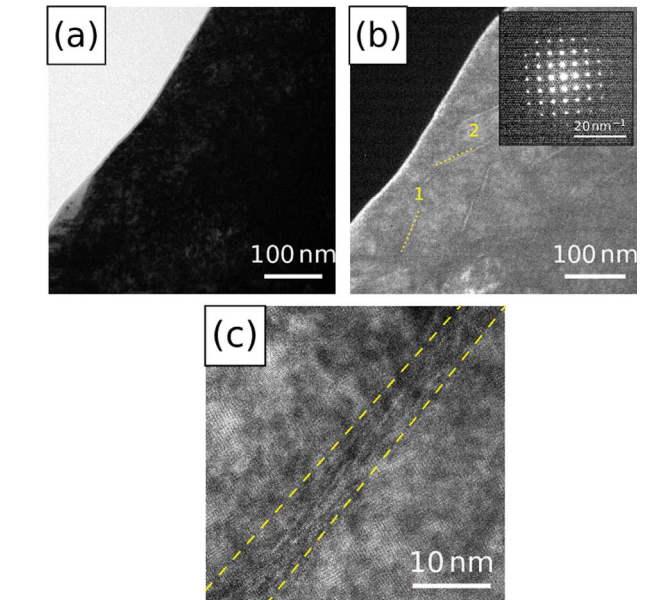


**Fig. 10.** Micrographs of alloy 16NiCrMo13 nitrided, quenched and submitted to cryogenic treatment : (a) bright field (BF) oriented in diffraction position, (b) same region but under dark field (DF) oriented according to the reflexion indicated in the diffraction pattern (DP) corresponding to the zone and (c) high resolution (HRTEM) detail of the  $Fe_{16}N_2$  zones depicted in (b). In (b) these shear zones composed of  $Fe_{16}N_2$  are identified by dotted lines and numbers. One of these regions is enclosed between dashed lines in (c), revealing their thickness of about 10 nm.

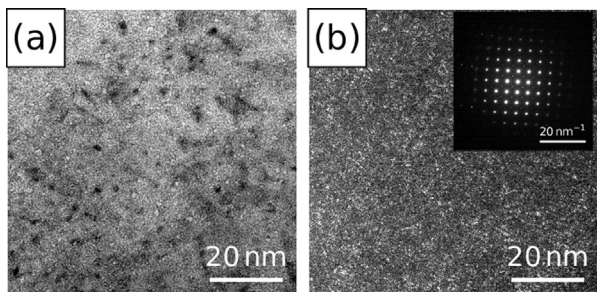


**Fig. 11.** Same sample as Fig. 10 but after tempering at 573 K : detail of the  $Fe_{16}N_2$  nanoprecipitates on (a) bright field (BF), (b) dark field (DF) and its respective SAED along  $[001]_\alpha$  in the represented area. Each clear spot in (b) represents an ordered region of  $Fe_{16}N_2$ .

drop is lower for carbonitriding than for carburizing in the nitrogen rich depth, this effect being fairly more pronounced for alloy 23MnCrMo5 for both temper conditions. Although the starting points for the treatments were identical (around 800 HV0.3 close to the surface), carbonitriding profiles produced hardness about 70 HV0.3 higher in the nitrogen-rich depth than carburizing alone for alloy 23MnCrMo5. Alloy 23MnCrMo5

has been enriched up to around 0.8 wt% N close to the surface, what under equilibrium conditions should decrease the amount of solid solution chromium by less than 0.3 wt% if one considers only the formation of MN nitrides. One might also expect lower martensite stability in agreement with the results by Grange et al. [38]. If we consider the precipitation of MnSiN<sub>2</sub> [5,6] also depleting the matrix from manganese, martensite becomes even more unstable. As per Catteau et al. [5], a state close to equilibrium is reached. Thus, tempering is governed by an impoverished iron-like matrix, for which the formation of incoherent Fe<sub>16</sub>N<sub>2</sub> is expected [8–14]. Nonetheless, these precipitates are known to lead to a maximum hardening during room temperature aging and lead to a hardness drop during tempering. It is proposed that the reminiscent alloying elements retard such coherent-to-incoherent transformation of Fe<sub>16</sub>N<sub>2</sub> observed in plain iron [43]. Furthermore, it must be emphasized that the equilibrium nitride under these conditions, Fe<sub>4</sub>N, has not been observed, supporting to the aforementioned model.

#### 3.4. Austenitic nitriding

Austenitic nitriding led to a different behavior when compared to both carburizing and carbonitriding. The introduction of only carbon or a combination of carbon and nitrogen led to hardness decrease in the whole profile after temper. Nitrided samples tend to maintain hardness close to the as-quenched state in the nitrogen rich layer if tempering is carried above a certain temperature. Even though the hold time was shorter for higher temperatures (Table 2), and according to Hollomon parameter giving time-temperature relations for tempering (Hollomon-Jaffe constant assumed equal to 20 [44,3]), stress relief with hardness drop along the profiles for all conditions was expected with increasing temperature, in contrast with experimental observations. Increasing tempering temperature to 673 K also maintains the hardness at the same level (Fig. 6). It is accompanied by the displacement of the hardness maximum toward the core and the hardness loss is more pronounced beyond nitrogen reach, such as depicted in Fig. 6. It is given by the increased nitrogen mobility and possible coalescence of precipitates at this temperature. These results imply a secondary precipitation happening during temper, which counterbalances hardness loss due to the relief of internal stresses. It is important to emphasize that hardness decrease is steeper for higher temperatures in zones beyond nitrogen reach, controlled by tempering of carbon-based martensite and confirming the hypothesis of precipitation during the stress relief treatment. This behavior may justify the improved hardness retention of carbonitriding over carburizing.

#### 3.5. Transmission electron microscopy

The structure of martensite was revealed by transmission electron microscopy studies for different treatment conditions and stages. Focus has been given on elemental redistribution due to the formation of high temperature nitrides. Austenitic nitriding of alloy 16NiCrMo13 led (Fig. 9) to a lath martensite structure with a typical lath width of 200–500 nm in a region containing about 0.13 wt% C and around 0.25 wt% N after quenching and cryogenic treatment. This feature is depicted in Fig. 9a by parallel dotted lines following the martensite lath boundaries. Small amounts of homogeneously distributed sub-micron precipitates formed at enrichment temperature are revealed by the contrast in these images. Fig. 9b identifies two of these particles, which are circumscribed and identified by numbers: particle 1 possibly lies in the lath depicted in Fig. 9a or its upper or lower boundary, since TEM images supply a volumetric image. These particles are confirmed to be nitrides with stoichiometry MN – where M is basically Cr – through the chemical cartographies presented in Fig. 8. These x-ray fluorescence maps show on the left column areas containing chromium by means of a high density of white spots. Their corresponding nitrogen-rich zones are shown on the right side: the atomic number effect makes the technique less sensitive to nitrogen. Some of the nitrides (1, 3, and 4 on Fig. 8) are put into evidence by both Cr and N x-ray fluorescence, while particle designed by the

number 2 cannot be distinguished from the matrix in the nitrogen distribution map. Such difficulties can be dealt with by using longer exposure times or thinner samples.<sup>4</sup> Additionally, low atomic number elements can be detected more easily by EELS analysis.

Globular as well as stud-like morphologies of MN precipitates were quantified to cover around 1.8–2.5% of the foils cross-sections while Thermo-Calc [21,22] predicts a volume fraction of 1.0% for the local composition. Once the areas from where chemical cartographies were taken have an average thickness of 80 nm and by assuming that all MN precipitates in the scanned volume are detected, a rough estimate of the volume fraction of this component around 0.8–1.0% can be obtained from image analyses, close enough to the predicted value and thus local equilibrium. This result provides validation to the assumptions made previously for the analysis of as-quenched hardness. Shearing zones of around 100×10 nm (Fig. 10c – inscribed in the area delimited by dashed lines) composed of Fe<sub>16</sub>N<sub>2</sub> as identified by diffraction pattern shown in Fig. 10b, which present some of these zones at lower magnification by dotted lines.

Analysis of Fig. 10 provided a base line to the study of tempered samples. For samples tempered at 573 K and above, homogeneous precipitation of a multitude of small – less than 5 nm Fe<sub>16</sub>N<sub>2</sub> particles in the BCC martensite matrix has been detected. These particles could explain the abnormal tempering behavior previously depicted in Fig. 6, given their size and coherence with the matrix. It is proposed that the depleted alloy matrix behaves as pure Fe but with retarded precipitation of Fe<sub>16</sub>N<sub>2</sub>, leading to the observed behavior. This could be linked to a mass action kinetic limitation due to low nitrogen content, which did not allow the precipitates to reach the stable Fe<sub>4</sub>N observed for a much higher nitrogen mass fraction even at 433 K by Kaplow et al. [8]. For as-quenched alloy 23MnCrMo5 containing 0.35 wt% C and 0.80 wt% N, contrast and chemical maps brought to light a higher amount of high temperature precipitates than for alloy 16NiCrMo5, as expected. These may be classified into spherical/ellipsoidal (numbers 1, 2, and 3 in Fig. 8) and cuboid morphologies (one of the particles on zone number 4 in Fig. 8). These nitrides have already been reported by Catteau et al. [6], who showed the precipitation of MN nitrides at grain boundaries of previous austenite and also homogeneously distributed in the matrix of alloy 23MnCrMo5, but no Si<sub>3</sub>N<sub>4</sub> (as predicted by Thermo-Calc [21,22], database TCFE7) has been found either in the present work or in Catteau et al. [6]. The authors [6] also report the presence of VN, not identified in the present work, and MnSiN<sub>2</sub> (space group Pna2<sub>1</sub> [30]) formed at 0.25 wt% N, what is relatively low when compared to nitrogen contents achieved in the present work. The presence of MnSiN<sub>2</sub> is confirmed in the present study (Fig. 7) but not predicted by thermodynamic calculations with the used database. Fig. 7 shows that the formation of large nitrides is accompanied by an important depletion of iron, as shown in regions identified by numbers 1 and 4, which coincide with nitrogen-rich portions on the material. This region 1 is associated with two nitrides: a MN-nitride, evidenced by number 2 on the chromium map, and MnSiN<sub>2</sub> identified on manganese and silicon cartographies by number 3. There are some areas, such as the one identified by number 4 that apparently form a mixed nitride, probably of stoichiometry MN with some chromium lattice points substituted by manganese. Finally, at region 5 of Fig. 7, a multitude of MN nitrides, the majority of them formed mostly of chromium (then close to CrN) are present.

#### 4. Conclusions

The present work showed that the hardening achieved through carbonitriding of low alloy steels may be predicted in terms of Norstrom [17] model if interstitial atoms are taken into account by mole fractions, allowing the inclusion of nitrogen in order to explain the as-quenched hardness. The use of computational thermodynamics software allowed the estimation of these quantities in austenite, which were considered relevant to martensite

<sup>4</sup> In the present work, FIB technique was used for sample removal and led to thicknesses around 80 nm, what imposed constraints to EDX analysis.

composition. Maximum hardening seems also related to the BCC to BCT structural transformation of martensite, being reflected to a total mass fraction of solid solution interstitials of 0.55 wt%, the known H-point [15]. Tempering led to a less pronounced hardness drop for carbonitriding than carburizing, evidencing a secondary precipitation mechanism. This result is also seen from austenitic nitriding, for which a minimum temperature for such precipitation was inferred. Transmission electron microscopy analyses showed that a fine homogeneous dispersion of  $\text{Fe}_{16}\text{N}_2$  is responsible for such comportment. The presence of alloying elements is probably retarding the coherent to incoherent transformation of these precipitates, allowing such secondary hardening behavior at around 573 K.

## Acknowledgments

The authors are grateful to CNRS and IRT M2P for the financial support. We would also like to acknowledge the companies Safran, PSA Peugeot Citroën, Faurecia, ECM Technologies, Ascometal, Air Liquide, Airbus Helicopters, Arcelor Mittal, UTC Aerospace Systems and Poclain Hydraulics for the supply of raw materials and financial support through IRT M2P. Special thanks to Mrs. Christine Gendarme from Institut Jean Lamour for the conduction on chemical microanalyses.

## References

- [1] J. Slycke, T. Ericsson, A study of reactions occurring during the carbonitriding process, *J. Heat Treat.* 2 (1981) 3–19. <http://dx.doi.org/10.1007/BF02833069>.
- [2] J. Slycke, T. Ericsson, A study of reactions occurring during the carbonitriding process part II, *J. Heat Treat.* 2 (1981) 97–112. <http://dx.doi.org/10.1007/BF02833226>.
- [3] G.E. Totten, *Steel Heat Treatment: Metallurgy and Technologies*, Taylor and Francis, 2006.
- [4] A.G. Khachaturyan, *Theory of Structural Transformations in Solids*, 1st ed., Dover Publications, 1983.
- [5] S.D. Catteau, S. Denis, J. Teixeira, J. Dulcy, M. Dehmas, A. Redjaiimia, M. Courteaux, Constitutive effects of carbon and nitrogen on isothermal transformations of austenite in a low alloy steel, in: Proceedings of the 21st Congress IFHTSE.
- [6] S. Catteau, H.V. Landeghem, J. Teixeira, J. Dulcy, M. Dehmas, S. Denis, A. Redjaiimia, M. Courteaux, Carbon and nitrogen effects on microstructure and kinetics associated with bainitic transformation in a low-alloyed steel, *J. Alloy. Compd.* 658 (2016) 832–838. <http://dx.doi.org/10.1016/j.jallcom.2015.11.007> (ISSN 0925-8388).
- [7] G. Krauss, Martensite in steel: strength and structure, *Mater. Sci. Eng.: A* 273–275 (0) (1999) 40–57. [http://dx.doi.org/10.1016/S0921-5093\(99\)00288-9](http://dx.doi.org/10.1016/S0921-5093(99)00288-9) (ISSN 0921-5093).
- [8] R. Kaplow, M. Ron, N. DeCristofaro, Mössbauer effect studies of tempered martensite, *Metall. Trans. A* 14 (6) (1983) 1135–1145. <http://dx.doi.org/10.1007/BF02670451> (ISSN 0360-2133).
- [9] A. Van Gent, F. Van Doorn, E. Mittemeijer, Crystallography and tempering behavior of iron-nitrogen martensite, *Metall. Trans. A* 16 (8) (1985) 1371–1384. <http://dx.doi.org/10.1007/BF02658670> (ISSN 0360-2133).
- [10] E. Mittemeijer, L. Cheng, P. van der Schaaf, C. Brakman, B. Korevaar, Analysis of nonisothermal transformation kinetics; tempering of iron-carbon and iron-nitrogen martensites, *Metall. Trans. A* 19 (4) (1988) 925–932. <http://dx.doi.org/10.1007/BF02628377> (ISSN 0360-2133).
- [11] L. Cheng, E. Mittemeijer, The tempering of iron-nitrogen martensite; dilatometric and calorimetric analysis, *Metall. Trans. A* 21 (1) (1990) 13–26. <http://dx.doi.org/10.1007/BF02656420> (ISSN 0360-2133).
- [12] L. Cheng, N. van der Pers, A. Böttger, T. de Keijser, E. Mittemeijer, Lattice changes of iron-nitrogen martensite on aging at room temperature, *Metall. Trans. A* 21 (11) (1990) 2857–2867. <http://dx.doi.org/10.1007/BF02647206> (ISSN 0360-2133).
- [13] I. Fall, J.-M. Genin, Mössbauer spectroscopy study of the aging and tempering of high nitrogen quenched Fe-N alloys: kinetics of formation of  $\text{Fe}_{16}\text{N}_2$  nitride by interstitial ordering in martensite, *Mater. Mater. Trans. A* 27 (8) (1996) 2160–2177. <http://dx.doi.org/10.1007/BF02651871> (ISSN 1073-5623).
- [14] M. Van Genderen, A. Böttger, E. Mittemeijer, Formation of  $\alpha''$  iron nitride in FeN martensite: nitrogen vacancies, iron-atom displacements, and misfit-strain energy, *Metall. Mater. Trans. A* 28 (1) (1997) 63–77. <http://dx.doi.org/10.1007/s11661-997-0083-9> (ISSN 1073-5623).
- [15] O.D. Sherby, J. Wadsworth, D.R. Lesuer, C.K. Syn, Revisiting the structure of martensite in iron-carbon steels, *Mater. Trans.* 49 (9) (2008) 2016–2027. <http://dx.doi.org/10.2320/matertrans.MRA2007338>.
- [16] M. Cohen, Strengthening Mechanisms in Steel, *Materials Transactions* 9 (Suppl.).
- [17] L.-A. Norstrom, On the yield strength of quenched low-carbon martensite, *Scand. J. Metall.* 5 (1976) 159–165.
- [18] B. Hutchinson, J. Hagström, O. Karlsson, D. Lindell, M. Tornberg, F. Lindberg, M. Thuvander, Microstructures and hardness of as-quenched martensites (0.1–0.5%), *Acta Mater.* 59 (14) (2011) 5845–5858. <http://dx.doi.org/10.1016/j.actamat.2011.05.061> (ISSN 1359-6454).
- [19] G. Ghosh, G. Olson, Simulation of paraequilibrium growth in multicomponent systems, *Metall. Mater. Trans. A* 32 (3) (2001) 455–467. <http://dx.doi.org/10.1007/s11661-001-0062-5> (ISSN 1073-5623).
- [20] L. Sproge, J. Ågren, Experimental and theoretical studies of gas consumption in the gas carburizing process, *J. Heat Treat.* 6 (1) (1988) 9–19. <http://dx.doi.org/10.1007/BF02833160> (ISSN 0190-9177).
- [21] J.-O. Andersson, T. Helander, L. Höglund, P. Shi, B. Sundman, Thermo-calc & dictra, computational tools for, *Mater. Sci., CALPHAD* 26 (2) (2002) 273–312. [http://dx.doi.org/10.1016/S0364-5916\(02\)00037-8](http://dx.doi.org/10.1016/S0364-5916(02)00037-8).
- [22] A. Borgenstam, A. Engström, L. Höglund, J.A. gren, DICTRA, a tool for simulation of diffusional transformations in alloys, *J. Phase Equilibil.* 21 (3) (2000) 269–280. <http://dx.doi.org/10.1361/105497100770340057>.
- [23] Y. hui Yang, M. qiu Wang, J. chao Chen, H. Dong, Microstructure and mechanical properties of gear steels after high temperature carburization, *J. Iron Steel Res., Int.* 20 (12) (2013) 140–145. [http://dx.doi.org/10.1016/S1006-706X\(13\)60227-7](http://dx.doi.org/10.1016/S1006-706X(13)60227-7) (ISSN 1006-706X).
- [24] J. Dulcy, M. Gantois, Théorie des traitements thermochimiques – Cémentation. Carburation., Techniques de l'ingénieur Traitements thermiques superficiels et thermochimiques base documentaire: TIB501DUO. (ref. article: m1222).
- [25] N. Loukachenko, *Mise au point de surfaces résistant à des sollicitations de roulement – Glissement sous des pressions de contact élevées de 2,5 GPa et jusqu'à 300 °C. Applications aux engrenages et aux transmissions par courroies* (Ph.D. thesis), Institut National Polytechnique de Lorraine, 2006.
- [26] E. Lehrer, Über das Eisen-Wasserstoff-Ammoniak-Gleichgewicht, *Z. Elektrochem.* 36 (1930) 383–392.
- [27] C. Chatfield, M. Hillert, A thermodynamical analysis of the Fe-Mo-c system between 973 and 1273 k, *Calphad* 1 (3) (1977) 201–223. [http://dx.doi.org/10.1016/0364-5916\(77\)90001-3](http://dx.doi.org/10.1016/0364-5916(77)90001-3) (ISSN 0364-5916).
- [28] M. Hillert, M. Waldenström, Isothermal sections of the Fe-Mn-C system in the temperature range 873 K-1373 K, *Calphad* 1 (2) (1977) 97–132. [http://dx.doi.org/10.1016/0364-5916\(77\)90013-X](http://dx.doi.org/10.1016/0364-5916(77)90013-X) (ISSN 0364-5916).
- [29] M. Hillert, C. Qiu, A thermodynamic assessment of the Fe-Cr-Ni-C system, *Mater. Trans. A* 22 (10) (1991) 2187–2198. <http://dx.doi.org/10.1007/BF02664985> (ISSN 1543-1940).
- [30] F. Weitzer, J. Schuster, Phase diagrams of the ternary systems Mn, Fe, Co, Ni-Si-N, *J. Solid State Chem.* 70 (2) (1987) 178–184. [http://dx.doi.org/10.1016/0022-4596\(87\)90054-5](http://dx.doi.org/10.1016/0022-4596(87)90054-5) (ISSN 0022-4596).
- [31] H.K.D.H. Bhadeshia, Carbon-carbon interactions in iron, *J. Mater. Sci.* 39 (2004) 3949–3955. <http://dx.doi.org/10.1023/B:JMSC.0000031476.21217.f4>.
- [32] K. Oda, H. Fujimura, H. Ino, Local interactions in carbon-carbon and carbon-M (M: Al, Mn, Ni) atomic pairs in FCC γ-iron, *J. Phys.: Condens. Matter* 6 (3) (1994) 679. <http://dx.doi.org/10.1088/0953-8984/6/3/008>.
- [33] A. Sozinov, A. Balanyuk, V. Gavriljuk, C-C interaction in iron-base austenite and interpretation of Mössbauer spectra, *Acta Mater.* 45 (1) (1997) 225–232. [http://dx.doi.org/10.1016/S1359-6454\(96\)00138-3](http://dx.doi.org/10.1016/S1359-6454(96)00138-3) (ISSN 1359-6454).
- [34] A. Sozinov, A. Balanyuk, V. Gavriljuk, N-N interaction and nitrogen activity in the iron base austenite, *Acta Mater.* 47 (3) (1999) 927–935. [http://dx.doi.org/10.1016/S1359-6454\(98\)00394-2](http://dx.doi.org/10.1016/S1359-6454(98)00394-2) (ISSN 1359-6454).
- [35] L. Onsager, Reciprocal relations in irreversible processes. I, *Phys. Rev.* 37 (1931) 405–426.
- [36] L. Onsager, Reciprocal relations in irreversible processes.II, *Phys. Rev.* 38 (1931) 2265–2279.
- [37] J. Crank, P. Nicolson, A practical method for Numerical evaluation of solutions of partial differential equations of the heat-conduction type, *Advances in Computational Mathematics*, 6, 1996, pp. 207–226, <http://dx.doi.org/10.1017/S0305004100023197> reprinted from Proc. Camb. Phil. Soc. 43, 1947, pp. 50–67.
- [38] R. Grange, C. Hribal, L. Porter, Hardness of tempered martensite in carbon and low-alloy steels, *Metall. Trans. A* 8 (11) (1977) 1775–1785. <http://dx.doi.org/10.1007/BF02646882> (ISSN 0360-2133).
- [39] P. Ferro, F. Bonollo, Modelling of the carburizing and quenching process applied to caterpillar track bushings, *Model. Simul. Mater. Sci. Eng.* 22 (2) (2014) 025019. <http://dx.doi.org/10.1088/0965-0393/22/2/025019>.
- [40] P. Haasen, Chapter 23 – Mechanical properties of solid solutions, in: R.W.C. Haasen (Ed.), *Physical Metallurgy* (Fourth Edition), North-Holland, Oxford, fourth edition edn., pp. 2009–2073, ISBN 978-0-444-89875-3. <http://dx.doi.org/10.1016/B978-044489875-3/50028-4>.
- [41] S. Morito, J. Nishikawa, T. Maki, Dislocation density within lath martensite in Fe-C and Fe-Ni alloys, *ISIJ Int.* 43 (9) (2003) 1475–1477. <http://dx.doi.org/10.2355/isijinternational.43.1475>.
- [42] M.-S. Yahia, Contribution à l'étude de l'influence de l'azote dans les traitements thermochimiques de surface des aciers en phase austénitique (Ph.D.thesis), Institut National Polytechnique de Lorraine, 1995.
- [43] E.J. Mittemeijer, *Fundamentals of Materials Science: The Microstructure-property Relationship Using Metals as Model Systems*, Springer, 2011. <http://dx.doi.org/10.1007/978-3-642-10500-5>.
- [44] N. Wan, W. Xiong, J. Suo, Mathematical model for tempering time effect on quenched steel based on hollomon parameter, *Journal of Materials Sciences and Technology* 21 (06), p. 803.